Full paper

Amino acid salt-driven planar hybrid perovskite solar cells with enhanced humidity stability

Seong-Cheol Yun, Sunihl Ma, Hyeok-Chan Kwon, Kyungmi Kim, Gyumin Jang, Hyunha Yang, Jooho Moon*

Department of Materials Science and Engineering, Yonsei University, 50 Yonsei-ro, Seodaemun-gu, Seoul 03722, Republic of Korea

ABSTRACT

While hybrid perovskites have great potential as light-absorbing materials, they suffer from moisture-induced instability. Herein, we added the amino acid iodide salt-based molecular crosslinker *p*-aminobenzoic acid (PABA·HI) to a perovskite precursor solution to enhance the humidity stability. The rigid molecular structure of PABA·HI played an important role in determining the crystal orientation, trap density, and photovoltaic performance of the perovskite solar cells (PVSCs). PABA·HI can effectively interact with the Pb-I framework via hydrogen bonds, enhancing the crosslinking efficiency compared with freely rotating flexible molecular crosslinkers. Kelvin probe force microscopy in conjunction with Raman analysis confirmed the presence of PABA·HI at the grain boundaries; thus, stable quasi-two-dimensional perovskite existed along the grain boundaries, passivating the grain boundaries and improving the moisture stability. The PABA·HI-added PVSCs having a power-conversion efficiency (PCE) of 17.4% retained 91% of their initial PCE when stored for 312 h at a relative humidity of 75% at 25 °C, whereas a pristine cell with a PCE of 16.4% only retained 37% of its initial value. Our findings clearly indicate that the amino acid salt as a rigid molecular crosslinker improved not only the photovoltaic performance but also the stability against moisture.

1. Introduction

Organic–inorganic hybrid perovskites (OIHPs) have received considerable attention as an absorber layer for photovoltaic devices owing to their unique optoelectrical properties, such as their suitable bandgap, large diffusion length, and high charge-carrier mobility [1–3]. Recently, the power-conversion efficiency (PCE) of OIHP-based solar cells reached 23.7% [4]. Furthermore, because of their low-cost fabrication process, earth-abundant elemental composition, and high PCE, tremendous effort has been directed towards the commercialization of OIHPs [5]. However, the commercialization of OIHPs faces critical issues arising from heat-, oxygen-, illumination-, and moisture-induced instabilities under operating conditions [6–9].

In particular, methylammonium lead triiodide (MAPbI$_3$) is vulnerable to a humid environment in which the organic cation (i.e., MA$^+$) having a hygroscopic nature adsorbs water molecules, forming either monohydrate or dihydrate [10]. Prolonged exposure to moisture results in the irreversible decomposition of perovskite into MAI and PbI$_2$ [10,11]. Recently, Wang et al. reported that amorphous grain boundaries in perovskite film allow fast diffusion of water molecules into

perovskite, initiating the degradation of OIHPs [12]. Therefore, a protection strategy, such as encapsulating the entire device or interface engineering, is necessary to avoid the diffusion of water molecules into perovskite grains [6,13]. Specifically, the interface between the perovskite and the hole transport layer was passivated by phenylalkylamine, in which the amine group anchors to the Pb-I framework of perovskite through hydrogen bonds. As a result, the benzene ring in the molecule forms a hydrophobic passivating layer that hampers the penetration of water molecules into the perovskite [14]. Furthermore, numerous materials have been applied to the encapsulation of OIHP-based solar cells [15]. However, the vulnerable intrinsic nature of the perovskite material under humidity is not changed by encapsulation or interfacial treatments, which hinders the practical application of MAPbI$_3$ for solar cells. To overcome these limitations, additive engineering of perovskite precursor solutions has been developed, and various additives—such as polymers, hydroiodic acid, fullerene derivatives, and organic molecules—have been suggested [16–19]. For example, butylphosphonic acid 4-ammonium chloride (4-ABPACl) and 5-aminovaleric acid (5-AVA) have been reported as crosslinkable additives whereby the neighboring perovskite grains are crosslinked with

* Corresponding author.
  E-mail address: jmoon@yonsei.ac.kr (J. Moon).

phosphonic acid and carboxylic acid, respectively, via hydrogen bonds [20,21]. These molecular crosslinkers were present at perovskite grain boundaries, hampering the water intrusion into the perovskite film. However, the carbon chains in both 4-ABPACl and 5-AVA comprise unsaturated single bonds, allowing the rotation of the molecules and thereby reducing the crosslinking efficiency [19]. In contrast to these flexible molecules, rigid molecules having crosslinkable moiety are more promising as effective crosslinking agents for passivating the perovskite grains without impairing the photovoltaic performance.

Herein, we report an attempt to improve the moisture stability of planar-structure perovskite solar cells (PVSCs) using amino acid salts with a π-conjugated benzene ring, such as *p*-aminobenzoic acid iodide (PABA·HI), as a crosslinker. Both the amino group and the carboxylic acid group in PABA·HI are capable of interacting with the Pb-I perovskite framework at grain boundaries through hydrogen bonds [22]. The rigid benzene ring allows the conformation of PABA·HI to be readily aligned, improving the crosslinking efficiency compared with flexible molecules having single carbon bonds [23]. Moreover, the presence of PABA·HI enhances the preferred orientation along the (110) direction of the perovskite film owing to the PABA·HI-induced oriented growth. Furthermore, the trap density of the perovskite thin films calculated using the space-charge-limited current (SCLC) method was reduced when PABA·HI was added. Thus, PABA·HI was present at the grain boundaries, functioning as a physical barrier to water intrusion into the perovskite films. Consequently, PABA·HI-added PVSCs exhibited a higher PCE (17.4%) than the pristine counterpart (16.4%). Remarkably, PABA·HI-added perovskite also exhibited improved stability in a high-humidity atmosphere (relative humidity (RH) = 75%) for 312 h.

2. Experimental section

2.1. Preparation of amino acid iodide

To prepare the amino acid iodide precursor, amino acid (*p*-aminobenzoic acid or γ-aminobutyric acid, Sigma–Aldrich, St. Louis, MO, USA) was dissolved in ethyl alcohol (anhydrous, ≥ 99.5%, Sigma–Aldrich). The solution was reacted with an equal molar amount of hydroiodic acid (57 wt% in H_2O, distilled, stabilized, 99.95%, Sigma–Aldrich) at 0 °C for 2 h. Amino acid iodide was recovered via vacuum drying at 50 °C for 2 h. The product was washed with diethyl ether several times and dried in a vacuum oven at 60 °C for 24 h.

2.2. Fabrication of PVSCs

FTO glass was cleaned using an ultrasonic bath for 30 min in ethanol. After partially taping the bottom electrode contact, UV treatment was conducted for 15 min. To fabricate the compact TiO_2 layer with a thickness of ∼ 40 nm, a solution of TiO_2 precursor (titanium isopropoxide, 99.999%, Sigma–Aldrich, 0.6134 mL) and an HCl solution (84 μL) in ethanol (8 mL) were spin-coated onto the cleaned FTO glass at 4000 rpm for 30 s, followed by drying at 100 °C for 10 min. The spin-coated substrates were annealed at 500 °C for 30 min in a box furnace. Then, compact TiO_2 coated substrates were subjected to $TiCl_4$ post-treatment. The compact TiO_2 substrates were soaked in a 0.02 M aqueous $TiCl_4$ (≥ 99%, Sigma–Aldrich) solution at 90 °C for 10 min. The substrate was immediately cleaned with deionized water and annealed at 500 °C for 30 min in the box furnace again. For the fabrication of the perovskite precursor solution, a 53 wt% mixture of PbI_2 (99.9985%, Alfa Aesar, MA, US), CH_3NH_3I (Greatcell solar, Queanbeyan, Australia), and dimethyl sulfoxide (Sigma–Aldrich) (1:1:1 M ratio) was dissolved in dimethylformamide (Sigma–Aldrich). To obtain additive-included perovskite precursors, several additives were added to the perovskite precursor solution. To fabricate the absorber layer, the precursor solution was spin-coated onto the TiO_2-coated substrates at 4000 rpm for 25 s. Diethyl ether (0.5 mL) was dripped onto the substrate at 16 s, prior

to the end of the spinning process. Immediately, the spin-coated substrates were dried at 65 °C for 3 min and annealed at 100 °C for 10 min, forming dark-brownish perovskite film with a thickness of ∼ 400 nm. The HTM solution was prepared by dissolving 72 mg of spiro-OMeTAD (Sigma–Aldrich) in 1 mL of chlorobenzene and adding 28.8 μL of 4-tert-butylpyridine (Sigma–Aldrich) and 17.5 μL of a Li salt solution (520 mg mL^{-1} lithium bis(trifluoromethylsulfonyl)imide in acetonitrile). For the fabrication of HTL layer with a thickness of ∼ 200 nm, the spiro-OMeTAD solution was spin-coated onto the perovskite layer at 3000 rpm for 30 s. Finally, a 70-nm-thick Au electrode layer was thermally evaporated onto the spiro-OMeTAD film.

2.3. Optical, structural, and electrical characterizations

The absorbances of the perovskite layers were measured using a UV–vis spectrophotometer (V-670, Jasco, Tokyo, Japan), and a soda lime glass substrate was used for the baseline measurement. The surface morphologies of the samples were analyzed using field-emission SEM (JSM-7001F, JEOL Ltd., Tokyo, Japan). KPFM (AFM, SPA 400, Seiko Instruments, Inc., Chiba, Japan) analysis was conducted using an Au-coated Si tip (SI-DF3-A, f = 23–31 kHz) to obtain topographic images and contact potential difference maps of the perovskite thin films without and with additives in the configuration of glass/FTO/compact TiO_2/perovskite. External open-circuit condition of DC bias was applied to the tips, where the FTO was grounded. All samples were measured under dark conditions. The crystallinity information of the films was obtained by using a high-resolution XRD instrument (Rigaku Smartlab, TX, USA). The SCLC measurement of the PVSCs was performed using a Keithley 2400 source measurement unit (Keithley Instruments Inc., Cleveland, OH, USA) under dark conditions. Raman spectra were measured by a Horiba Jobin-Yvon LabRAM ARAMIS spectrometer using an Nd: Aag laser beam at the excitation wavelength of 532 nm. The active area of the PVSCs was 0.40 cm^2. *J–V* scanning was performed over the range of 0.1–2.0 V with a dwell time of 50 ms at each point. IS was measured using a frequency-response analyzer (1252 A, Solartron, Bogner Regis, England) while applying an oscillation of 10 mA (alternating current) at a frequency in the range of 0.1 Hz–0.3 MHz under 1-sun illumination. Steady-state PL decay transients were measured at 770 nm while excitation wavelength of 470 nm was used. TRPL measurements were obtained using an inverted-type scanning confocal microscope (MicroTime-200, Picoquant, Germany) with a 40× objective. A single-mode pulsed diode laser (470 nm, with a pulse width of ∼30 ps, average power of ∼0.1 μW, and repetition rate of 0.5 MHz) was utilized as excitation source. To measure the emissions from the samples, a dichroic mirror (490 DCXR, AHF), a long-pass filter (HQ500lp, AHF), a 100-μm pinhole, a bandpass filter (FB760, Thorlabs), and a single-photon avalanche diode (PDM series, MPD) were used.

2.4. Characterization of photovoltaic properties

The photovoltaic performance of the PVSCs was measured by using a solar simulator (Sol3A Class AAA, Oriel Instruments, Stratford, CT, USA) and a Keithley 2400 source measurement unit (Keithley Instruments Inc., Cleveland, OH, USA) under AM 1.5 and 1-sun (100 mW cm^{-2}) conditions. A standard Si reference cell certified by the Newport Corporation (Irvine, CA, USA) was used for calibration of the 1-sun intensity. The active area of the PVSCs was 0.06 cm^2, as determined by the aperture mask. Scanning was performed over the range of − 0.1–1.2 V at a rate of 0.52 V s^{-1} with a dwell time of 50 ms at each point. For the *J–V* hysteresis measurement, scanning was performed at a rate of 0.048 V s^{-1} with a dwell time of 300 ms. The EQE was determined using a quantum efficiency measurement system (QEX10, PV Measurements, Inc.).
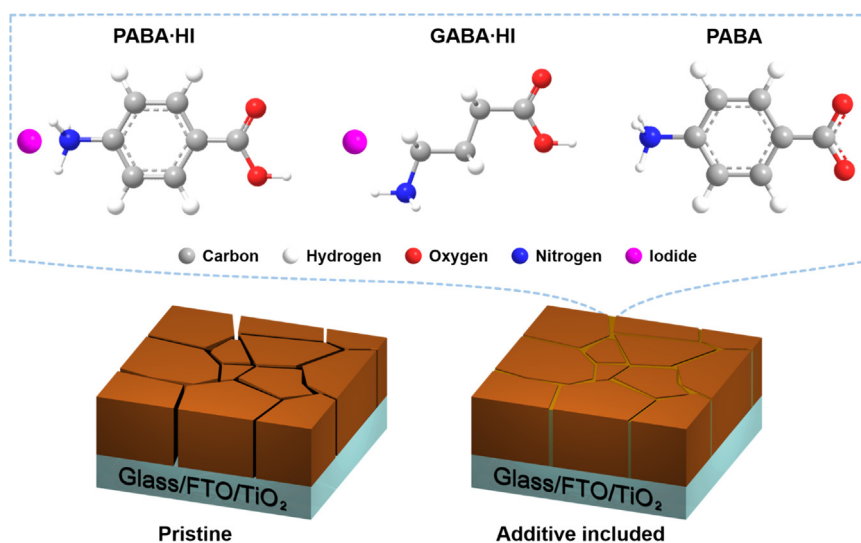
Scheme 1. Schematic representation of the pristine and additive-included perovskite thin films, as well as the molecular structures of the three additives: PABA·HI, GABA·HI, and PABA.

2.5. Stability test

Humidity stability tests were performed on the PVSCs in a temperature- and humidity-controlled chamber (TH-PE-025, Jeol Tech, Seoul, Republic of Korea) at constant RH level of 40–75% and temperature of 25–40 °C in dark conditions. Half-cell samples with the configuration of glass/FTO/compact TiO_2/perovskite without and with additives were placed inside the controller chamber, being exposed to the moist air. The humidity chamber was opened and the samples were removed after a designated exposure time for UV–vis spectroscopy, XRD, and *J–V* analysis.

3. Results and discussion

To verify the role of the molecular structure of the additives to address the intrinsic instability issue of perovskites against moisture, we introduced three different amino acid additives—PABA·HI, γ-aminobenzoic acid iodide (GABA·HI), and *p*-aminobenzoic acid (PABA)—into the perovskite precursor solutions, as shown in Scheme 1 (upper image). Although these molecules have similar carbon chain lengths and molecular sizes, PABA and PABA·HI have a rigid conformation compared with the flexible GABA owing to the π-π conjugated benzene ring in the PABA molecule. Perovskite thin films were prepared on glass/fluorine-doped tin oxide (FTO)/compact TiO_2 via an antisolvent-assisted spin-coating method using perovskite precursor solutions without and with additives whose molar amount was similar to that in recent studies [19,24]. Top-view scanning electron microscopy (SEM) images showed that regardless of the additive type, there was no significant difference in the grain structures among four different perovskite films in which the grain size was approximately 400 nm (Fig. S1). Thus, amino acid or amino acid iodide additives have no influence on the morphology and grain size of perovskite films.

X-ray diffraction (XRD) measurement was performed to evaluate the effect of additives on the perovskite crystal quality (Fig. 1a). The XRD results of all four perovskite thin films without and with amino acid or amino acid iodide salt showed identical peaks at 14.12°, 28.44°, 31.87°, and 40.5°, corresponding to the (110), (220), (310), and (224) planes of the $MAPbI_3$ perovskite structure, respectively [24]. Zhu et al. recently reported the increased preferred orientation of perovskite thin films, showing the enhanced peak intensity ratio of the (110) plane to the (310) plane [25]. To identify the difference of the preferred crystal orientation among the samples, the peak intensity ratios of the (110) plane to the (310) plane were compared (Fig. 1b). The PABA·HI-added

perovskite exhibited the highest peak intensity ratio, whereas the perovskites with GABA·HI and PABA had similar intensity ratios to the pristine perovskite. These results indicate that PABA·HI in the perovskite precursor induces preferential growth of the (110) perovskite plane, whereas GABA·HI and PABA have no such effect on the crystal growth. The structure of the crosslinking agents plays an important role in the perovskite crystal formation [26]. A slight molecular modification, such as the varying chain length of alkyl phosphonic acids, causes significantly different crosslinking behavior because the change of the molecular structure leads to a different alignment of the functional groups of additives with respect to the perovskite crystal orientation [20,26]. All amino acid-based additives contain two functional groups—carboxylic acid and amino groups—oppositely located at the two ends of each molecule (Scheme 1), both of which can interact with the Pb-I framework via hydrogen bonds, leading to crosslinking between the neighboring perovskite grains [27,28]. However, molecular rigidity and flexibility can affect the crystal orientation among the crosslinked perovskite grains [22]. The amino end of GABA·HI obliquely points toward the perovskite crystal surface owing to its molecular flexibility when carboxylic acid interacts with the Pb-I framework. Thus, GABA·HI cannot induce preferred oriented perovskite crystal growth (Scheme 2a).

To gain an in-depth understanding of the crosslinking efficiency depending on the additive molecular structure, Raman spectroscopy was performed on four samples—pristine $MAPbI_3$, $MAPbI_3$ + PABA·HI, $MAPbI_3$ + GABA·HI, and $MAPbI_3$ + PABA films—as shown in Fig. 1c. In order to avoid laser-induced degradation of perovskite during measurement, low laser intensities and short acquisition time were applied to the freshly prepared samples. All samples exhibited the characteristic peaks of the Pb-I framework at 64 and 94 cm^{-1}, corresponding to Pb-I bending and stretching, respectively. A peak at 114 cm^{-1} was also observed, which corresponded to the coupled libration mode of MA$^+$ with the Pb-I framework [29,30]. Interestingly, only the peak intensity at 114 cm^{-1} varied depending on the additive type. Senanayak et al. have shown that the reduction of a peak around 114 cm^{-1} is correlated with the decreased interaction between MA$^+$ and the Pb-I framework, suggesting more ordered growth of $MAPbI_3$ films on the substrate, as seen in our XRD results [30]. The PABA·HI-added perovskite film showed the lowest peak intensity at 114 cm^{-1}. The reduced intensity at 114 cm^{-1} was due to the reduced interaction between MA$^+$ and the Pb-I framework. Effective crosslinking with the neighboring Pb-I framework in the perovskite likely diminishes the libration mode of the MA$^+$ cation, as MA$^+$ is replaced by amino acid-based additives. This indicates
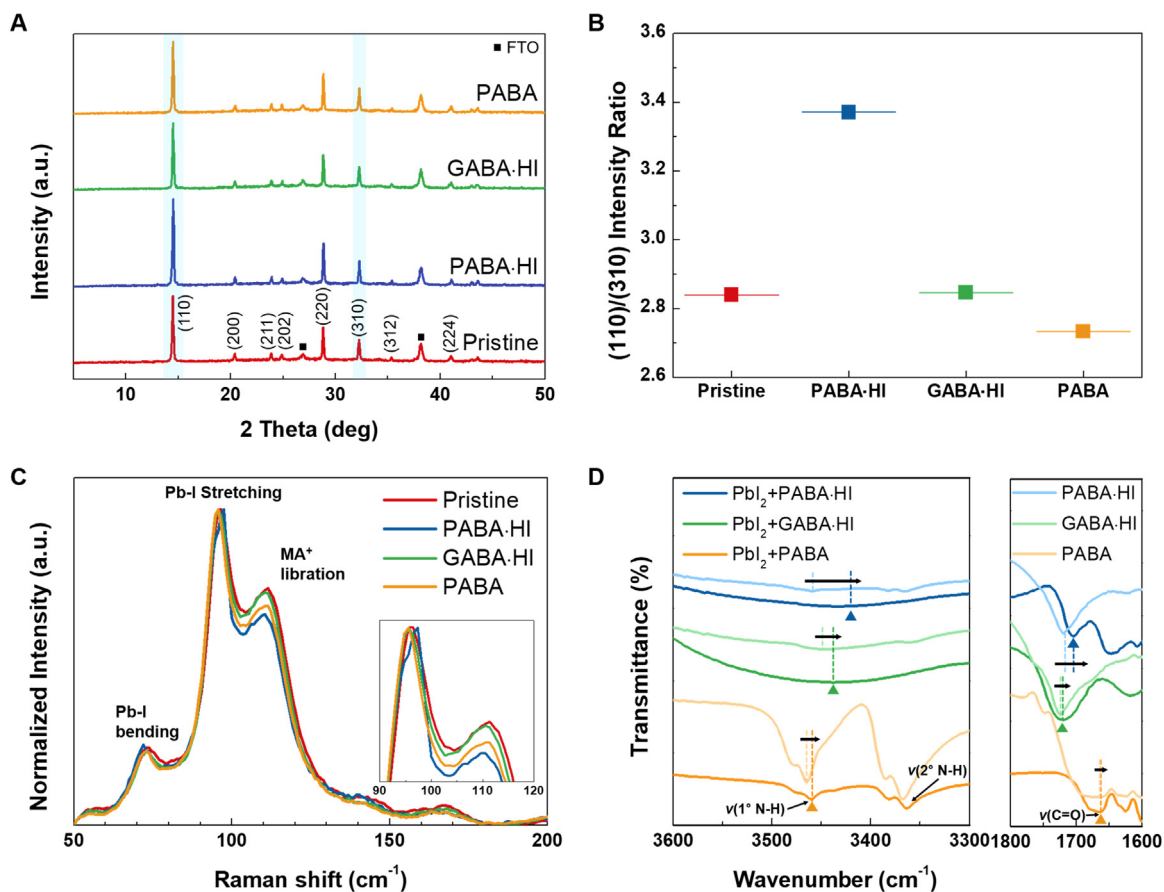
Fig. 1. (a) XRD results and (b) the peak intensity ratio of the (110) plane to the (310) plane for four different perovskite thin films without and with additives. The peak intensity was normalized to the peak of the FTO substrate. (c) Surface Raman spectroscopy of perovskite thin films without and with additives. The inset presents the magnified region of 90–120 cm^{-1}. (d) FT-IR spectroscopy of PbI$_2$ + PABA·HI, PbI$_2$ + GABA·HI, PbI$_2$ + PABA, PABA·HI, GABA·HI, and PABA powders in the range from 3600–3300 cm^{-1} and 1800–1600 cm^{-1}.
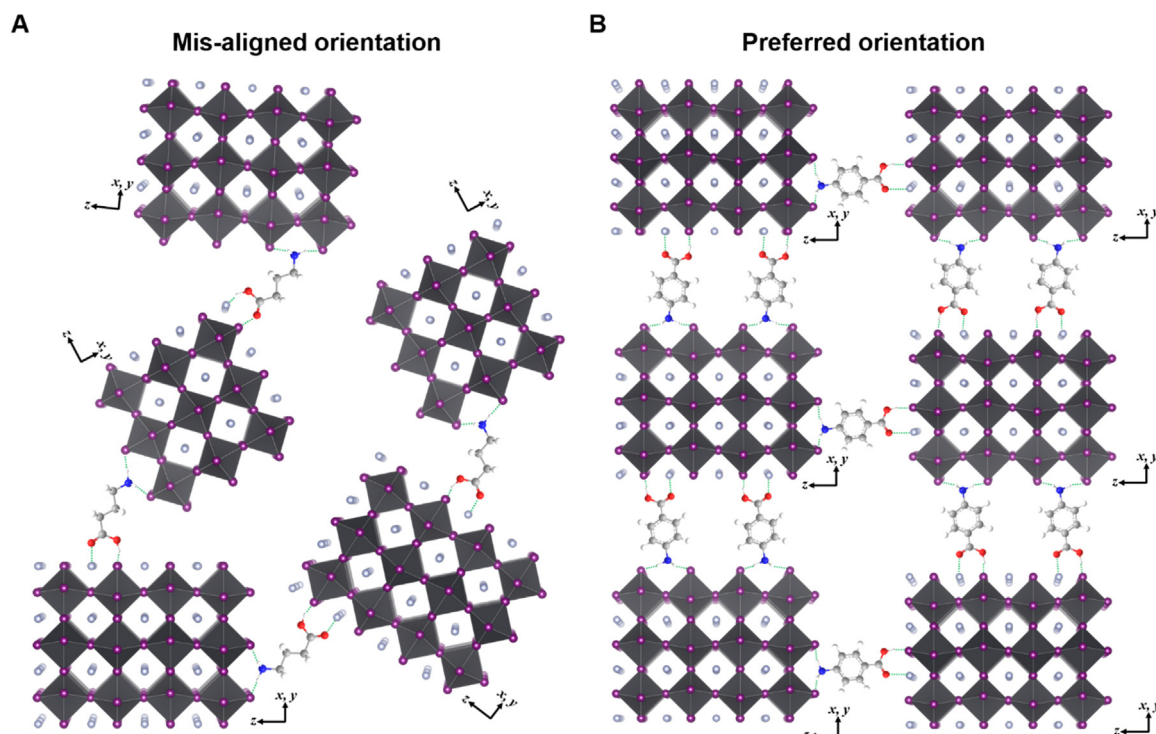
Scheme 2. Schematic crosslinking behavior of (a) the flexible molecule GABA·HI and (b) the rigid molecule PABA·HI between neighboring perovskite crystals. The PABA·HI induces the preferred orientation growth of perovskite.

that the PABA·HI molecule interacted with the Pb-I framework more effectively than GABA·HI or PABA when the same molar amounts of the additives were added to the perovskite thin films.

Fourier transform infrared spectroscopy (FT-IR) was performed on PbI_2 + PABA·HI, PbI_2 + GABA·HI, PbI_2 + PABA, PABA·HI, GABA·HI, and PABA powders to precisely compare the crosslinking ability of each additive toward the Pb-I framework without the hindrance of MAI since the abundant ammonium cations already exist on the perovskite (Fig. 1d). The absorption peaks (triangular mark) around $3400 \, cm^{-1}$ are attributed to the stretching mode of the N-H bond in the amino group that interacts with the Pb-I framework [31]. Unlike PbI_2 + PABA·HI and PbI_2 + GABA·HI, PbI_2 + PABA exhibited another peak at $3364 \, cm^{-1}$, which can be assigned to the 2° N-H stretching mode in the molecule. The peak at $3364 \, cm^{-1}$ indicates the unprotonated amino group in the PABA molecules. Moreover, the broadening of the absorption peak for PbI_2 + PABA·HI and PbI_2 + GABA·HI due to the stretching mode of -OH in the carboxylic acid was observed, reflecting the protonation of carboxylic acid in both PABA·HI and GABA·HI, whereas the PABA retained unprotonated carboxylic acid. The main absorption peak corresponding to the 1° N-H stretching mode occurred at $3435 \, cm^{-1}$ for PbI_2 + PABA·HI, $3438 \, cm^{-1}$ for PbI_2 + GABA·HI, and $3460 \, cm^{-1}$ for PbI_2 + PABA, whereas the absorption peak of PABA·HI, GABA·HI, and PABA showed at $3450 \, cm^{-1}$, $3448 \, cm^{-1}$, and $3464 \, cm^{-1}$, respectively. The absorption peak shift into the lower region of N-H stretching mode means the existence of an interaction between the amino end of additives and Pb-I framework [31,32]. Notably, in the case of PbI_2 + PABA·HI, the greater shift to the lower wavenumber region compared with PbI_2 + GABA·HI and PbI_2 + PABA indicates the stronger interaction of PABA·HI with the Pb-I framework. Similar phenomenon is also observed in carboxylic acid group of additives as observed in the interaction between amino group and Pb-I framework. The characteristic absorption peak of C=O stretching mode occurred at around $1690 \pm 50 \, cm^{-1}$ [19]. The PbI_2 + PABA·HI sample showed a peak shift to $1703 \, cm^{-1}$ from $1710 \, cm^{-1}$ for PABA·HI. Meanwhile, the PbI_2 + GABA·HI sample revealed a peak at $1720 \, cm^{-1}$, whereas the peak of GABA·HI appeared at $1724 \, cm^{-1}$. Accordingly, the carboxylic end of PABA·HI has stronger interaction than GABA·HI. On the other hand, the absorption peak of PbI_2 + PABA sample occurred at $1662 \, cm^{-1}$. As for PbI_2 + PABA, the carboxylic end of PABA interacts in the form of $-COO^-$ with Pb-I framework rather than -COOH due to zwitterionic behavior of amino acid. The lone electron pair at C=O bond shuttles to neighboring C-O bond, forming resonance structure. Therefore, the vibration between C=O bonds becomes weakened, reflecting lowered C=O absorption peak as compared with others. The absorption peak of C=O stretching bond in PABA occurred at $1663 \, cm^{-1}$, which was shifted to $1662 \, cm^{-1}$ for PbI_2 + PABA. This indicates that the interaction between $-COO^-$ end of PABA and Pb-I framework is insignificant. Additionally, the evidence for the interaction between carboxylic end and Pb-I framework could be provided by FT-IR measurement around $1400 \, cm^{-1}$ wavenumber region because the in-plane bend mode of -OH can be assigned to this range [33]. As shown in Fig. S2, the characteristic peak of -OH was observable for PbI_2 + PABA·HI and PbI_2 + GABA·HI, whereas PbI_2 + PABA showed no peak around this range. Thus, it can be found that the interaction between PABA·HI and GA-BA·HI with Pb-I framework is mainly due to the hydrogen bonding. On the other hand, the carboxylic end in PABA could not afford proper interaction with Pb-I framework due to the zwitterionic behavior as shown in Fig. 1d and S2. Consequently, PABA·HI, which has the rigid molecular structure and both protonated functional groups, reveals the most efficient crosslinking efficiency with Pb-I framework, enabling the well-aligned preferential orientation in perovskite crystal growth (Scheme 2b), as exhibited by the enhanced peak intensity ratio of the (110)/(310) plane (Fig. 1b).

PVSCs were fabricated with the device configuration of glass/FTO/ compact TiO_2/MAPbI$_3$ without and with additives/spiro-OMeTAD/Au in order to examine the effect of the molecular structure of the additives. Full device structures are shown in Fig. S3. The compact TiO_2 and spiro-OMeTAD act as electron and hole transport layers, respectively. The corresponding current density–voltage (J–V) curves, external quantum efficiencies (EQEs), statistical distributions, and photovoltaic parameters are shown in Fig. S4 and Table S1. The best-performing PVSCs were obtained when PABA·HI was used as a crosslinker, showing a PCE of 17.4%, an open-circuit voltage (V_{OC}) of 1.08 V, a current density (J_{SC}) of $20.7 \, mA \, cm^{-2}$, and a fill factor (FF) of 77.6%. In contrast, the PVSCs with GABA·HI and PABA exhibited inferior photovoltaic performance, with lower V_{OC} and FF, whereas the J_{SC} was similar regardless of the additive. The similar J_{SC} is attributed to the analogous surface morphology regardless of the additive type, as shown in Fig. S1 [34]. To determine the V_{OC} and FF for the various additives, the steady-state photoluminescence (PL) was measured. The perovskite samples with the incorporation of either GABA·HI or PABA exhibited lower PL intensities than the pristine perovskite (Fig. S5). The energy loss of the PVSCs under the operating condition is mainly attributed to defect-induced nonradiative recombination [16]. The PL results suggest that the molecular conformation not only affects the crosslinking efficiency but also influences the defect state of perovskite films. The waggling end of the flexible molecule GABA·HI and the unprotonated carboxylic end of PABA may act as trap sites inside the perovskite, reducing the PL intensities [35]. On the contrary, the PABA·HI-added perovskite thin films showed a higher PL intensity than the pristine perovskite (Fig. S5). The firmly crosslinked PABA·HI between the perovskite grains may passivate the trap site. Furthermore, the higher FF value is attributed to the preferred (110) crystal orientation due to the more crosslinkable rigid PABA·HI [36]. Therefore, the enhanced V_{OC} and FF resulted in an improved PCE for the PABA·HI-added PVSCs. Considering the effects on the crystallographic structure and PCE, the PABA·HI additive was selected as an effective molecular crosslinker for the perovskite thin film.

The influence of the PABA·HI addition amount on the perovskite crystal was investigated using XRD measurement (Fig. S6a). All samples without the additive and with varying amounts of the additive showed nearly identical diffraction patterns, indicating negligible disturbance of the perovskite phase formation by PABA·HI. No peak corresponding to PbI_2 or PABA·HI was observed, suggesting that the PbI_2 was completely converted into perovskite crystals and there was no agglomeration of PABA·HI [10]. The incorporation of PABA·HI into the perovskite precursor increased the peak intensity ratio of the (110) plane to the (310) plane, which was maximized with the addition of $5 \, mg \, mL^{-1}$ PABA·HI (Fig. S6b), indicating preferential growth in the (110) direction, as described in Scheme 2b. The increased XRD intensity ratio is mainly determined by the crystal growth mechanism [37,38]. Because the interactions between PABA·HI and MAI or PbI_2 are present in our system, when more additives are introduced in the precursor solution, further retarded growth is expected, showing high peak intensity ratio of the (110) plane to the (310) plane. Therefore, the interaction between PABA·HI and perovskite precursor is responsible for retarded crystal growth and resulting preferred growth of perovskite. It is noteworthy that the grain size for $5 \, mg \, mL^{-1}$ of PABA·HI added perovskite in the top-view SEM images showed smaller grain size than others (Fig. S7). This is because PABA·HI can also influence the nucleation rate of perovskite phase. The carboxylic end of PABA·HI can interact with TiO_2, while the amino group acts as a nucleation seed during the perovskite layer formation [22]. Thus, when the PABA·HI was added more than $5 \, mg \, mL^{-1}$, the grain size would become further small due to the presence of abundant nucleation seeds. Nonetheless, the differences in both XRD intensity ratio and morphology between $5 \, mg \, mL^{-1}$ and $10 \, mg \, mL^{-1}$ added perovskites were nearly insignificant. This saturated grain size dependency upon the addition of PABA·HI can be explained in terms of molecular interaction between PABA·HI. Because PABA·HI has π-conjugated benzene ring, the nearby PABA·HI can interact with each other by π-π stacking [39]. When more than $5 \, mg \, mL^{-1}$ of PABA·HI is introduced to perovskite precursor, this molecular interaction makes

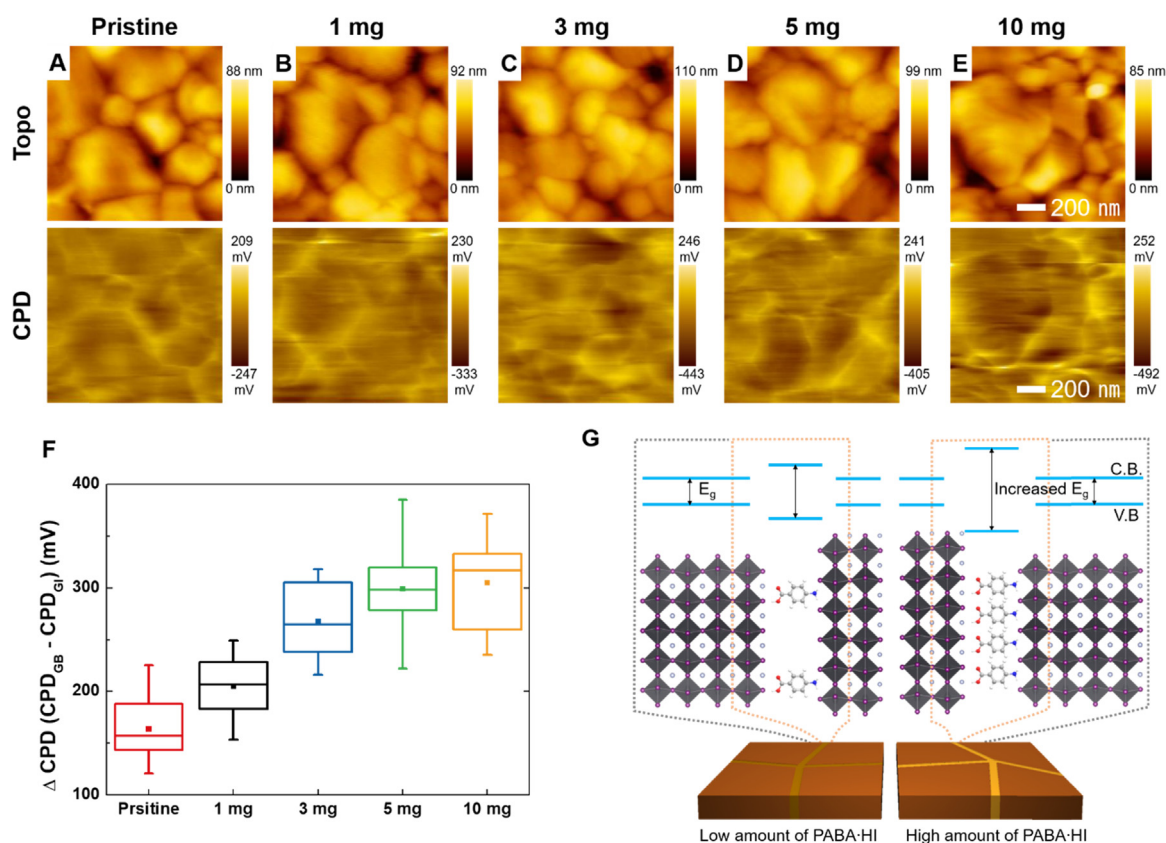**Fig. 2.** Topological images and corresponding CPD maps of (a) pristine perovskite and (b) 1 mg mL^{-1}, (c) 3 mg mL^{-1}, (d) 5 mg mL^{-1}, and (e) 10 mg mL^{-1} PABA·HI-added perovskite thin films. (f) CPD difference between the grain boundaries and grain interiors according to the incorporation of PABA·HI. (g) Schematic band diagram and relevant crystal structure of the perovskite. The quasi-2D perovskite forms at the grain boundaries owing to the addition of PABA·HI, whereas the grain interiors maintain 3D perovskite. The quasi-2D perovskite increases the bandgap at the grain boundary compared with the grain interior, and the addition of PABA·HI increases the bandgap at the grain boundary.

PABA·HI unable to retard the crystal growth without providing nucleation seeds. Accordingly, there were no variations in both preferred orientation growth and microstructure when more than 5 mg mL^{-1} of PABA·HI was introduced. The ultraviolet–visible (UV–vis) absorption spectra for the perovskite films with varying amounts of PABA·HI were obtained for measuring the optical properties (Fig. S8). Although the addition of PABA·HI changed the morphology, no obvious changes in the absorbance or absorption edge were observed.

To verify the existence of PABA·HI in the perovskite thin films, Kelvin probe force microscopy (KPFM) was performed for a sample with a configuration of glass/FTO/compact TiO$_2$/perovskite thin film without PABA·HI and with varying amounts of PABA·HI. KPFM is useful for measuring local electrical properties, such as the contact potential difference (CPD), as well as morphological features, providing nanoscale spatial information regarding thin-film surfaces [40,41]. The change in the work function for the surface of the measured sample is reflected by the difference in the CPD. Thus, a higher CPD indicates a higher work function in local regions. Fig. 2**a–e** show topographic images and corresponding CPD maps of perovskite thin films without PABA·HI and with different amounts of PABA·HI. When measured in the dark condition, the CPD at the grain boundaries was higher than that in the grain interior, as indicated by the bright outline. The averaged difference between the grain boundary and grain interior (i.e., ΔCPD = CPD$_{GB}$ - CPD$_{GI}$) is plotted in Fig. 2**f**. The ΔCPD was gradually increased from 160 mV for pristine perovskite to 300 mV for 10 mg mL^{-1} PABA·HI-added perovskite. This result indicates that the work-function difference increased owing to the presence of hydrogen-bonded PABA·HI at the grain boundaries, as confirmed by FT-IR (Fig. 1**d**). Recently, the existence of quasi-two-dimensional (2D) perovskite at the

grain boundaries was confirmed when molecular additives were added to the perovskite precursor [40]. The formation of quasi-2D perovskite at the grain boundaries is allowable owing to the larger size of PABA·HI compared with the methylammonium ion [42]. Moreover, hydrogen bonding between the amino group (i.e., -NH$_3$$^+$) and the Pb-I framework and the coordination of carboxylic acid (i.e., -COOH) with Pb and I atoms allow quasi-2D perovskite formation [27]. The increased addition of PABA·HI to the perovskite precursor led to an increased number of PABA·HI molecules located at the grain boundaries, increasing the ratio of quasi-2D perovskite. Accordingly, the increased amount of quasi-2D perovskite at the grain boundary likely resulted in the increase in ΔCPD, because 2D perovskite has a higher bandgap energy than three-dimensional (3D) perovskite, as schematically depicted in Fig. 2**g.**

To confirm the formation of quasi-2D perovskite at the grain boundaries, UV–vis absorption spectra for 3D perovskite (i.e., MAPbI$_3$), 2D perovskite (i.e., PABA$_2$PbI$_4$), and a mixture of these two perovskites were measured (Fig. S9). The pure 2D perovskite exhibited two peaks at 320 and 400 nm owing to its wider bandgap compared with the pure 3D perovskite [42]. The 2D/3D perovskite mixture at 3 mol% 2D perovskite had a similar absorption curve to the pure 3D perovskite. However, the 2D perovskite with more than 20 mol% clearly exhibited a transition in the absorption curve. As indicated by the XRD and UV–vis absorption (Fig. S6 and S8), the presence of < 3 mol% 2D perovskite was unable to alter the overall 3D perovskite structure. Thus, the grain interiors macroscopically exhibited the same properties as 3D perovskite. Nonetheless, the CPD difference observed via KPFM indicates the formation of quasi-2D perovskite at the grain boundaries. Hence, it can be concluded that the quasi-2D perovskite forms only at the grain boundaries when < 10 mg mL^{-1} (i.e., 1.19 mol%) PABA·HI is
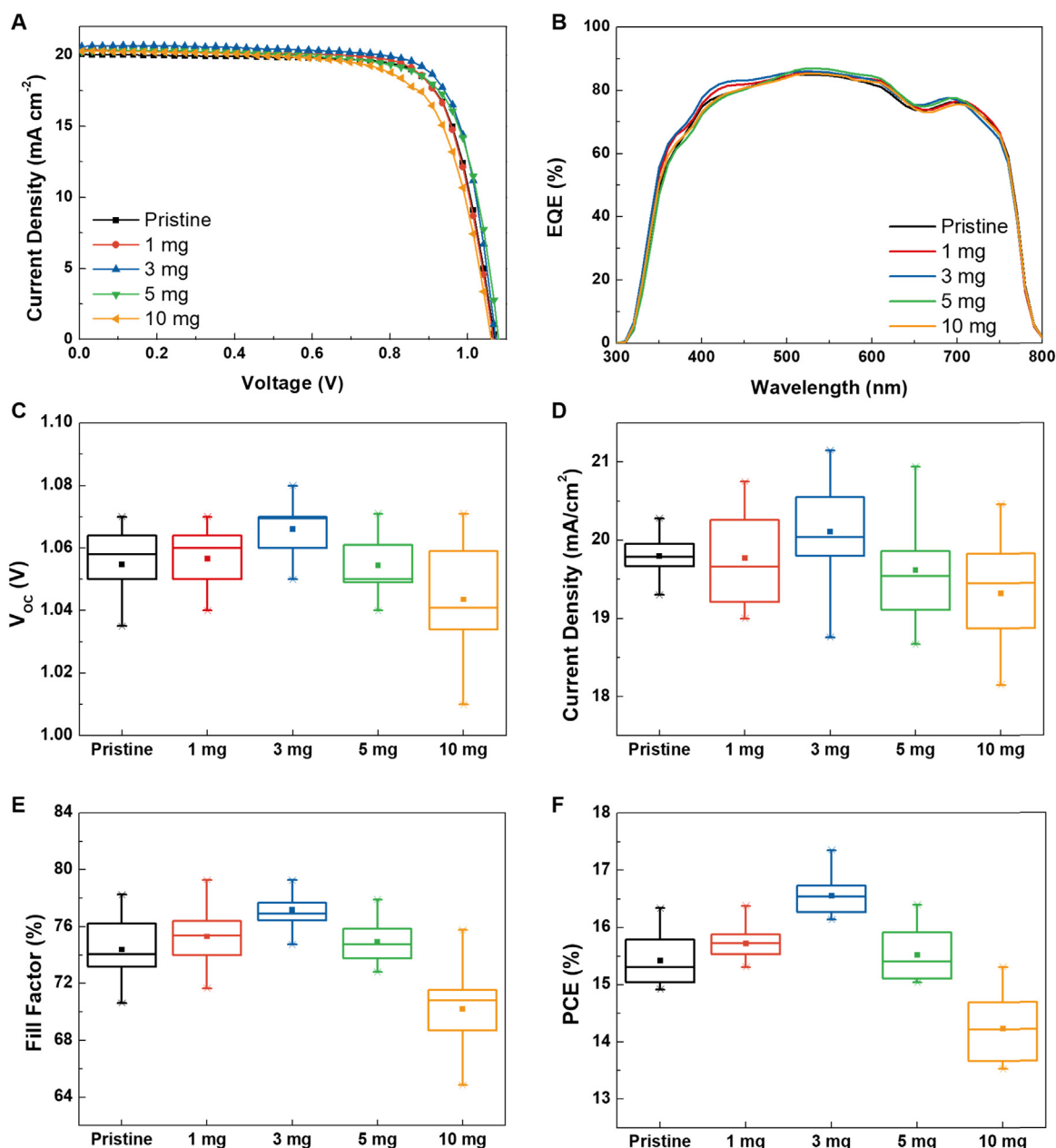
Fig. 3. (a) Photovoltaic performance and (b) corresponding EQE. The statistical distributions of the device parameters: (c) open-circuit voltage (V_{OC}), (d) current density (J_{SC}), (e) FF, and (f) PCE of PVSCs without PABA·HI and with different amounts of PABA·HI. The statistical values were obtained from 30 cells for each condition. The horizontal lines in the box represent the 25%, 50% and 75% of the devices. The squares mark (■) indicate the average values and the cross marks (×) show the maximum and minimum values.

added to the perovskite film.

The PVSCs without PABA·HI and with varying amounts of PABA·HI were fabricated in order to evaluate the effect of PABA·HI on the device performance. The J–V curve and the corresponding EQE of each device, as well as the corresponding statistics of the photovoltaic parameters, are presented in Fig. 3 and Table 1. The J_{SC} values calculated from the EQE spectra are listed in Table S2 and are similar to the J_{SC} values observed from the J–V curve. The observed J_{SC} had similar values regardless of the PABA·HI addition amount. The invariance in the UV–vis absorption likely contributed to the similar J_{SC} values. On the contrary, both the V_{OC} and FF were increased with the increase of the addition amount, except for the case of 10 mg mL^{-1} addition. These increases likely resulted from both trap site passivation and (110) plane preferred crystal growth, which can facilitate charge transfer into the charge transport layers [36]. However, the addition of excessive PABA·HI led

Table 1

Photovoltaic performance of the PVSCs according to the amount of PABA·HI added to the perovskite precursors.

Amount of PABA·HI (mg mL^{-1})	V_{OC} (V)	J_{SC} (mA cm^{-2})	FF (%)	PCE (%)
0	1.07	20.05	76.24	16.34
1	1.07	20.38	75.37	16.38
3	1.08	20.70	77.62	17.35
5	1.08	20.28	75.00	16.40
10	1.06	20.28	71.26	15.31

to an increased portion of quasi-2D perovskite at the grain boundaries, resulting in a bandgap widening at the grain boundaries. The increased bandgap across the grain boundaries likely hindered the charge transport through the perovskite grains, reducing both the FF and V_{OC} [40].

The addition of $3\,mg\,mL^{-1}$ PABA·HI to the precursor solution yielded the most improved best-performing PCE of 17.4%. Less PABA·HI incorporation presumably caused imperfect passivation, whereas excess PABA·HI could result in inferior charge transport. The perovskite thin films with the addition of $3\,mg\,mL^{-1}$ PABA·HI were further investigated to elucidate the superior photovoltaic performance. The hysteresis behavior of PVSCs without and with PABA·HI was evaluated by performing forward and backward scans, as presented in Fig. S10 and Table S3. The hysteresis index (HI) was calculated as follows:

$$HI = \frac{J_{RS}(0.7V_{OC})\text{-}J_{FS}(0.7V_{OC})}{J_{RS}(0.7V_{OC})}, \tag{1}$$

where $J_{RS}(0.7V_{OC})$ and $J_{FS}(0.7V_{OC})$ represent the current densities at 70% of the V_{OC} for the reverse and forward scans, respectively. The PVSCs with PABA·HI exhibited less hysteresis behavior (HI = 0.12) than the pristine PVSCs (HI = 0.17). The hysteresis of PVSCs mainly originates from defect-assisted ion migration [43]. Thus, the decreased hysteresis implies reduced defects inside the PABA·HI-added perovskite films. To confirm the reliability of the PVSCs, the stabilized current density and PCE at the maximum power of each cell were measured, as shown in Fig. S11. The pristine PVSCs exhibited a current density and efficiency of $17.1\,mA\,cm^{-2}$ and 15.0%, respectively, under a forward bias voltage of 0.88 V. The PVSCs with PABA·HI exhibited a stabilized current density and PCE of $17.7\,mA\,cm^{-2}$ and 16.2%, respectively, at a forward bias voltage of 0.91 V. This PCE value is similar to that obtained from the J–V curve.

SCLC measurement was performed on glass/FTO/perovskite without and with the PABA·HI/Au structure. As shown in Fig. 4a, three different regions were identified by the different values of the exponent n ($J \propto V^n$): the ohmic region for $n = 1$, the SCLC region for $n = 2$, and the trap-filled limited (TFL) region for $n > 3$ [44]. In the TFL region,

all the trap states are filled by the injected carriers. The voltage of the crossover point between the ohmic and TFL regions is the trap-filled limit voltage (V_{TFL}) and can be used to determine the trap density, as follows:

$$N_t = \frac{2\varepsilon_0 \varepsilon_r V_{TFL}}{qL^2}, \tag{2}$$

where ε_0 is the vacuum permittivity, ε_r is the relative dielectric constant, q is the elemental charge, and L is the thickness of the film [45]. The V_{TFL} of perovskite thin films without and with PABA·HI was 1.30 and 0.86 V, respectively. The calculated trap densities of perovskite thin films without and with PABA·HI were 2.91×10^{16} and 1.92×10^{16} cm^{-3}, respectively, which are similar to recently reported values [45]. It is well-known that vacancies at the perovskite surface are easily formed because of the low Gibbs formation energy and can act as charge trap sites [8,46]. With the addition of PABA·HI to perovskite precursors, the two functional groups of PABA·HI passivate the vacancy defects at the perovskite surfaces [47]. Accordingly, the trap density inside the PABA·HI-added perovskite film was lower than that of the pristine counterpart, as indicated by calculations using the SCLC method.

Impedance spectroscopy (IS) provides insight into the charge transport and recombination kinetics information. The recombination resistance (R_{REC}) and the charge-transfer resistance (R_{CT}) at the perovskite/charge transfer layer can be evaluated [43]. Nyquist plots of PVSCs without and with PABA·HI under 1-sun illumination (AM 1.5, $100\,mW\,cm^{-2}$) at a bias of 0.7 V, as well as an equivalent circuit, are shown in Fig. 4b. Similar to other perovskite-based solar cells, two semicircles are clearly observed: the semicircle in the high-frequency region is related to the charge-transfer resistance (R_{CT}). and the incomplete semicircle in the low-frequency region is related to the recombination resistance (R_{REC}). It has been reported that the series
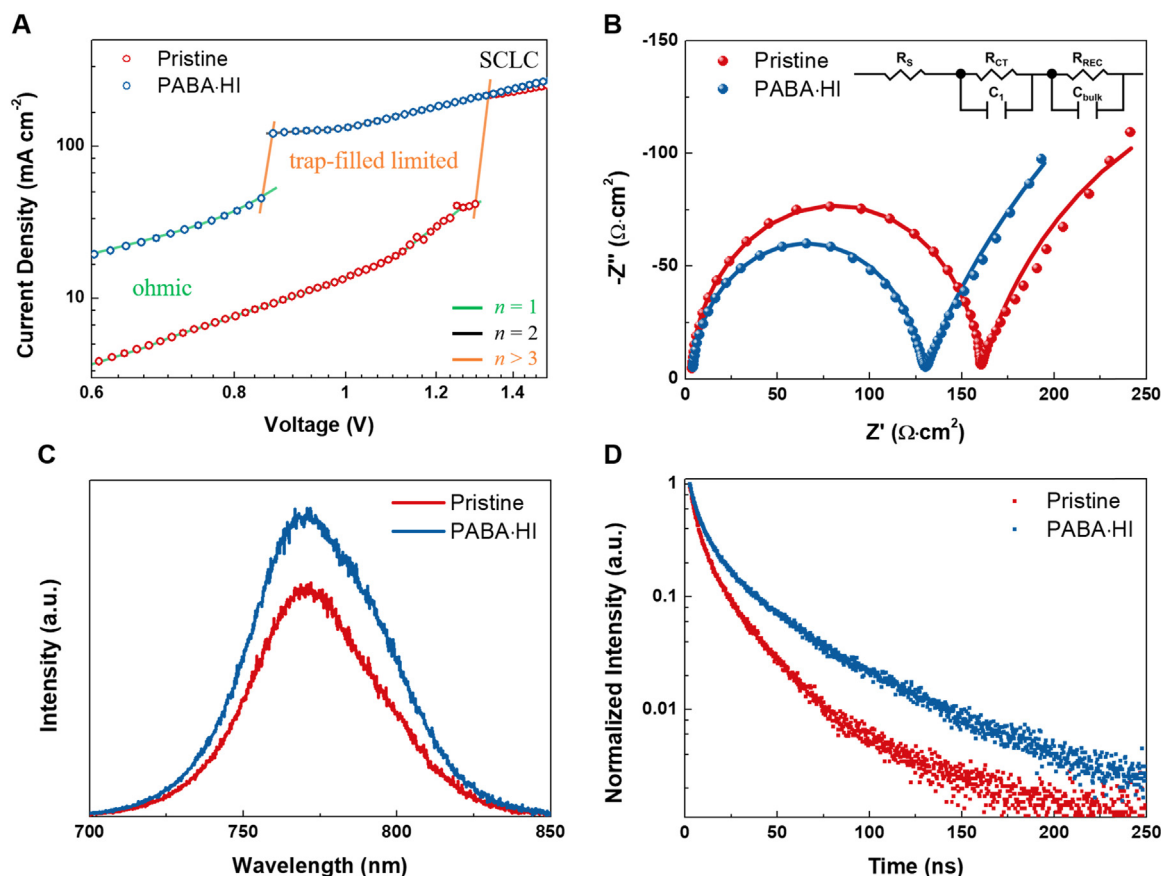

Fig. 4. (a) SCLC measurement of FTO/perovskite without and with the PABA·HI/Au structure. (b) Nyquist plot of pristine and PABA·HI-added PVSCs. (c) Steady-state PL and (d) TRPL spectroscopy for a configuration of glass/perovskite without and with PABA·HI.

resistance (R_S) reflects the resistances of the electrodes and external circuits, which is determined by the intercept at the real axis (Z'). R_{CT} reflects the resistance at the interfaces of the perovskite layer, and R_{REC} is mainly attributed to the recombination resistance between the perovskite film and the TiO$_2$ layer [34]. A previously reported equivalent circuit model for the PVSC was employed to fit these Nyquist plots [45]. The fitting parameters obtained using the equivalent circuit model are presented in Table S4. The R_S values of both PVSCs were similar (approximately $3\,\Omega\,cm^2$), indicating the good stacking of the individual component layers in the solar-cell devices. Unlike the R_S, the R_{CT} of the PABA·HI-added PVSC was lower than that of the pristine PVSC. The decreased R_{CT} is consistent with the enhanced (110) preferred orientation, which facilitated the charge transfer at the interfaces and increased the FF of the PABA·HI-added PVSC [36]. In contrast, the R_{REC} of the PABA·HI-added PVSC was higher than that of the pristine PVSC. The increase in R_{REC} indicates a reduction in the charge-carrier recombination, which is mainly attributed to the reduced defect density.

The steady-state PL emission intensity for perovskite film with the configuration of glass/perovskite is mainly determined by the recombination of the charge carriers (Fig. 4c) [34]. The PABA·HI-added perovskite exhibited a higher PL intensity than the pristine counterpart. This indicates that the inclusion of PABA·HI in the perovskite reduced the nonradiative decay rate owing to the reduced defect density [16]. Time-resolved PL (TRPL) spectra are presented in Fig. 4d. The TRPL results were fitted using a biexponential function to evaluate the decay lifetimes, as shown in Table S5 [48]. The pristine perovskite film exhibited fast (τ_1) and slow (τ_2) decay lifetimes of $\tau_1 = 3.46$ ns and $\tau_2 = 19.09$ ns, respectively, while the PABA·HI-added perovskite exhibited $\tau_1 = 5.30$ ns and $\tau_2 = 33.88$ ns. The τ_1 and τ_2 represent nonradiative recombination due to surface trap defects and radiative recombination from the bulk perovskite, respectively. Therefore, the increased decay lifetime suggests less trap-mediated recombination, indicating a lower trap density inside the PABA·HI-added perovskite. It is obvious from the PL measurement that the enhanced crosslinking efficiency of PABA·HI within the perovskite hindered the surface trap-mediated nonradiative recombination. This result is consistent with the SCLC and IS measurements. Therefore, both the V_{OC} and FF of the PABA·HI-added PVSCs were increased owing to the reduced energy loss originating from the reduced nonradiative recombination and effective charge transport.

The vulnerability of the perovskite layer at high humidity is the main obstacle for the commercialization of PVSCs. For a humidity stress test, half-cell devices (FTO/compact TiO$_2$/either pristine perovskite or PABA·HI-added perovskite without HTM) were placed in the dark at 25 °C and a RH of 75%. The RH of 75% is a relatively harsh condition for hygroscopic MAPbI$_3$ thin films, as the degradation of MAPbI$_3$ can be accelerated when the RH is $>$ 50% [11]. After a certain exposure time, the changes in the UV–vis absorption curve and crystallographic information were measured, as shown in Fig. 5a and b. The absorption curve of the PABA·HI-added perovskite films maintained its original shape, while a slight decrease was observed with prolonged exposure. On the other hand, the absorption curve of the pristine perovskite became flattened after the exposure to moisture, which is similar to other reports [49]. The degradation of both perovskites is compared in Fig. S12. The pristine perovskite thin film exposed to high humidity was decomposed into yellowish PbI$_2$, while the PABA·HI-added perovskite thin film maintained its original dark brownish color. This decomposition was confirmed by XRD measurement (Fig. 5b). The pristine perovskite thin film turned into perovskite dihydrate and PbI$_2$ after exposure to the RH 75% condition for 240 h. The PABA·HI-added perovskite thin film exhibited a slight peak of PbI$_2$, maintaining its original main peak at 14.12°. This suggests the perfect preservation of the perovskite layer even in the high-humidity environment.

To evaluate the effect of humidity on the photovoltaic performance, spiro-OMeTAD and Au layers were deposited on the half-cell sample after exposure to the humid environment (RH 75%) for completion of the PVSC full cells. Fig. 5c and Fig. S13 show the normalized PCE and
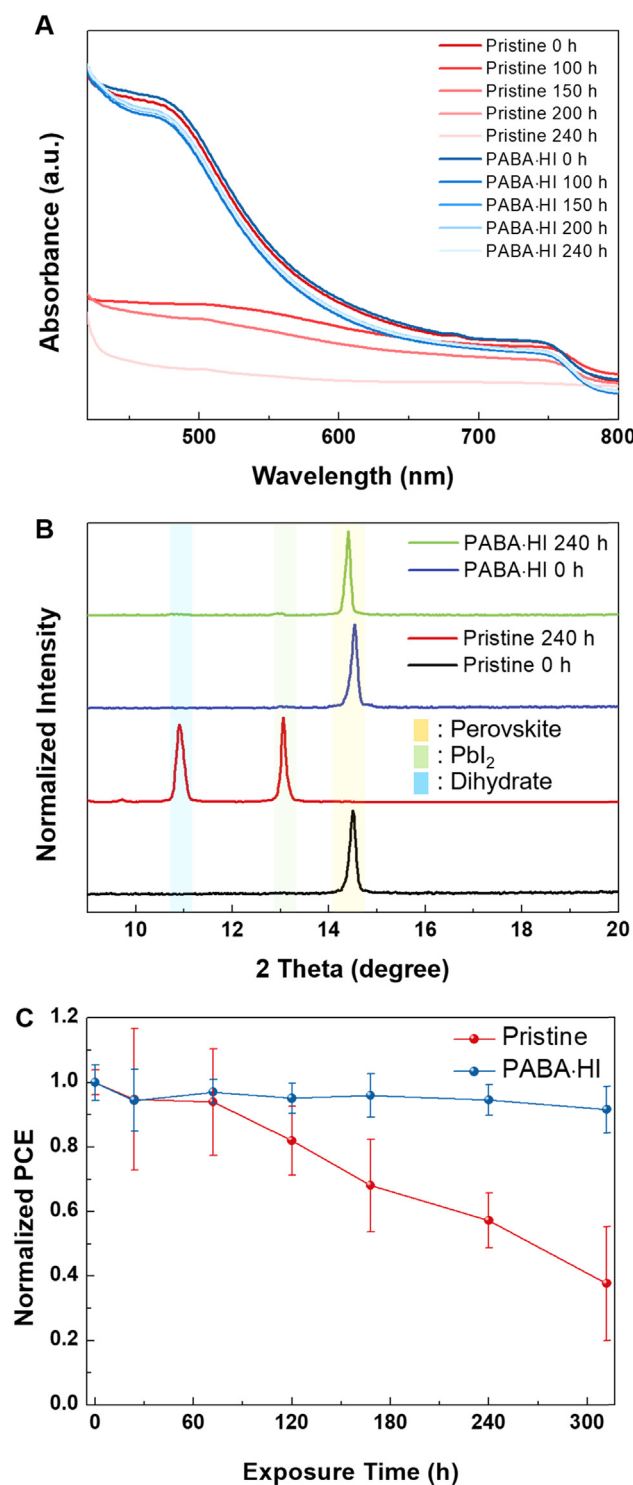
Fig. 5. (a) Variations of the UV–vis absorption and (b) XRD measurement of perovskite without and with PABA·HI under an RH of 75% at 25 °C in dark conditions with respect to the exposure duration. (c) Normalized PCE as a function of the exposure duration. The perovskite half-cells (glass/FTO/perovskite without and with PABA·HI) were exposed to an RH of 75% at 25 °C in dark conditions. After exposure for a designated duration, the HTM and the Au electrode were deposited prior to the measurement.

photovoltaic performance parameters as a function of exposure time under the high-humidity condition. The PVSCs with PABA·HI maintained 96% of original PCE value even after 168 h, while the PCE of pristine PVSCs decreased to approximately 68% of its initial value after

168 h of exposure. Furthermore, the PABA·HI-added PVSCs retained 91% of their initial PCE after 312 h of exposure. Similar stability was also observed when both half-cell samples were placed to elevated temperature humid air (40 °C, RH 40%) as shown in Fig. S14. The deteriorated PCE for the pristine PVSCs likely originated from the decomposition of perovskite into lead iodide. Leguy et al. reported that the perovskite layer was converted into monohydrate or dihydrate regardless of the film depth, because H_2O molecules easily diffused into the perovskite layer along the grain boundaries and the continuous exposure to high humidity fully converted the perovskite into PbI_2 [10]. H_2O molecules can permeate and spread through the grain boundaries of pristine perovskite films, eventually causing degradation [12]. On the contrary, the PABA·HI-enhanced stability against moisture is attributed to the microscopically formed quasi-2D perovskite at the grain boundaries. As confirmed by the KPFM results, PABA·HI was mainly located at the grain boundaries, forming quasi-2D perovskite (Fig. 4**g**). Quasi-2D perovskite is known to be more stable than 3D perovskite in a high-humidity environment [21]. The PABA·HI located at the grain boundaries of perovskite is also capable of crosslinking the adjacent grains. Thus, PABA·HI molecules can physically block grain boundaries, hampering water penetration. Notably, our PABA·HI additive significantly improved the stability against moisture, even under a high-humidity condition (RH 75%), compared with previous reports (Table S6). This clearly suggests that PABA·HI can serve as an effective molecular crosslinker that enhances the stability of perovskites against moisture.

4. Conclusions

We proposed the addition of PABA·HI to a perovskite precursor solution for the fabrication of perovskite thin films in order to improve the stability against moisture, as well as the PCE. The PABA·HI effectively interacted with the Pb-I framework through hydrogen bonds owing to the rigid molecular conformation, whereby (110) preferred grain growth occurred, while flexible counterparts deteriorated the crosslinking efficiency owing to the waggling molecular structure. Furthermore, the PABA·HI-added perovskite thin films exhibited a lower defect density and increased carrier lifetime than pristine perovskite thin films because the functional groups of PABA·HI readily passivated the trap sites. Notably, KPFM and FT-IR results indicated that PABA·HI molecules were located at the grain boundaries of the perovskite thin film, forming quasi-2D perovskite along the grain boundaries. The presence of PABA·HI in conjunction with humidity-stable quasi-2D perovskite at the grain boundaries significantly enhanced the stability of the perovskite phase against moisture. Hence, the PABA·HI-added perovskite thin film nearly maintained its initial PCE when exposed to a RH 75% atmosphere for 168 h and retained 91% of its original PCE after 312 h of exposure. In contrast, the PCE of the pristine perovskite thin film was abruptly degraded to 37% of its initial value after 312 h of exposure. Our research suggests that the molecular structure is an important selection criterion for the molecular crosslinker to simultaneously improve the efficiency and stability of PVSCs.

Acknowledgements

Appendix A. Supporting information

Supplementary data associated with this article can be found in the online version at doi:10.1016/j.nanoen.2019.02.064.

References

[1] J.-H. Im, C.-R. Lee, J.-W. Lee, S.-W. Park, N.-G. Park, Nanoscale 3 (2011) 4088.
[2] S.D. Stranks, G.E. Eperon, G. Grancini, C. Menelaou, M.J. Alcocer, T. Leijtens, L.M. Herz, A. Petrozza, H.J. Snaith, Science 342 (2013) 341.
[3] E. Edri, S. Kirmayer, A. Henning, S. Mukhopadhyay, K. Gartsman, Y. Rosenwaks, G. Hodes, D. Cahen, Nano Lett. 14 (2014) 1000.
[4] National Renewable Energy Laboratory USA, Best research-cell efficiencies. ⟨https://www.nrel.gov/pv/assets/pdfs/best-reserch-cell-efficiencies.pdf⟩, 2019 (Accessed 8 February 2019).
[5] M. Grätzel, Nat. Mater. 13 (2014) 838.
[6] N.H. Tiep, Z.L. Ku, H.J. Fan, Adv. Energy Mater. 6 (2016) 1501420.
[7] T. Leijtens, G.E. Eperon, N.K. Noel, S.N. Habisreutinger, A. Petrozza, H.J. Snaith, Adv. Energy Mater. 5 (2015) 1500963.
[8] N. Aristidou, C. Eames, I. Sanchez-Molina, X. Bu, J. Kosco, M.S. Islam, S.A. Haque, Nat. Commun. 8 (2017) 15218.
[9] H.S. Kim, J.Y. Seo, N.G. Park, ChemSusChem 9 (2016) 2528.
[10] A. l.M. Leguy, Y. Hu, M. Campoy-Quiles, M.I. Alonso, O.J. Weber, P. Azarhoosh, M. Van Schilfgaarde, M.T. Weller, T. Bein, J. Nelson, Chem. Mater. 27 (2015) 3397.
[11] J.L. Yang, B.D. Siempelkamp, D.Y. Liu, T.L. Kelly, ACS Nano 9 (2015) 1955.
[12] Q. Wang, B. Chen, Y. Liu, Y. Deng, Y. Bai, Q. Dong, J. Huang, Energy Environ. Sci. 10 (2017) 516.
[13] J. Huang, S. Tan, P.D. Lund, H. Zhou, Energy Environ. Sci. 10 (2017) 2284.
[14] F. Wang, W. Geng, Y. Zhou, H.H. Fang, C.J. Tong, M.A. Loi, L.M. Liu, N. Zhao, Adv. Mater. 28 (2016) 9986.
[15] J. Chen, X. Cai, D. Yang, D. Song, J. Wang, J. Jiang, A. Ma, S. Lv, M.Z. Hu, C. Ni, J. Power Sources 355 (2017) 98.
[16] L. Zuo, H. Guo, S. Jariwala, N. De Marco, S. Dong, R. DeBlock, D.S. Ginger, B. Dunn, M. Wang, Y. Yang, Sci. Adv. 3 (2017) e1700106.
[17] G.E. Eperon, S.D. Stranks, C. Menelaou, M.B. Johnston, L.M. Herz, H.J. Snaith, Energy Environ. Sci. 7 (2014) 982.
[18] Y. Zhang, P. Wang, X. Yu, J. Xie, X. Sun, H. Wang, J. Huang, L. Xu, C. Cui, M. Lei, J. Mater. Chem. A 4 (2016) 18509.
[19] X. Hou, S. Huang, W. Ou-Yang, L. Pan, Z. Sun, X. Chen, ACS Appl. Mater. Interfaces 9 (2017) 35200.
[20] X. Li, M.I. Dar, C. Yi, J. Luo, M. Tschumi, S.M. Zakeeruddin, M.K. Nazeeruddin, H. Han, M. Grätzel, Nat. Chem. 7 (2015) 703.
[21] G. Grancini, C. Roldán-Carmona, I. Zimmermann, E. Mosconi, X. Lee, D. Martineau, S. Narbey, F. Oswald, F. De Angelis, M. Graetzel, Nat. Commun. 8 (2017) 15684.
[22] C. Zhang, S. Zhang, X. Miao, Y. Hu, L. Staaden, G. Jia, Part. Part. Syst. Char. 34 (2017) 1600298.
[23] R. Koole, B. Luijges, M. Tachiya, R. Pool, T. Vlugt, C. de Mello Donegá, A. Meijerink, D. Vanmaekelbergh, J. Phys. Chem. C 111 (2007) 11208.
[24] J.-W. Lee, H.-S. Kim, N.-G. Park, Acc. Chem. Res. 49 (2016) 311.
[25] W. Zhu, L. Kang, T. Yu, B. Lv, Y. Wang, X. Chen, X. Wang, Y. Zhou, Z. Zou, ACS Appl. Mater. Interfaces 9 (2017) 6104.
[26] L. Zhang, L. Xu, F. Yu, J. Li, J. Mater. Chem. C 6 (2018) 234.
[27] T. Zhang, L. Xie, L. Chen, N. Guo, G. Li, Z. Tian, B. Mao, Y. Zhao, Adv. Funct. Mater. 27 (2017) 1603568.
[28] Y.C. Shih, Y.B. Lan, C.S. Li, H.C. Hsieh, L. Wang, C.I. Wu, K.F. Lin, Small 13 (2017) 10.
[29] Z. Liang, S. Zhang, X. Xu, N. Wang, J. Wang, X. Wang, Z. Bi, G. Xu, N. Yuan, J. Ding, RSC Adv. 5 (2015) 60562.
[30] S.P. Senanayak, B. Yang, T.H. Thomas, N. Giesbrecht, W. Huang, E. Gann, B. Nair, K. Goedel, S. Guha, X. Moya, Sci. Adv. 3 (2017) e1601935.
[31] H. Zhu, F. Zhang, Y. Xiao, S. Wang, X. Li, J. Mater. Chem. A 6 (2018) 4971.
[32] Y. Sun, Y. Wu, X. Fang, L. Xu, Z. Ma, Y. Lu, W.-H. Zhang, Q. Yu, N. Yuan, J. Ding, J. Mater. Chem. A 5 (2017) 1374.
[33] S. Olsztynska-Janus, K. Szymborska-Małek, M. Gasior-Glogowska, T. Walski, M. Komorowska, W. Witkiewicz, C. Pezowicz, M. Kobielarz, S. Szotek, Acta Bioeng. Biomech. 14 (2012) 101.
[34] J. Chen, S.G. Kim, N.G. Park, Adv. Mater. 30 (2018) 1801948.
[35] Y. Ogomi, A. Morita, S. Tsukamoto, T. Saitho, Q. Shen, T. Toyoda, K. Yoshino, S.S. Pandey, T.L. Ma, S. Hayase, J. Phys. Chem. C 118 (2014) 16651.
[36] L.K. Ono, Y. Qi, J. Phys. Chem. Lett. 7 (2016) 4764.
[37] D. Bi, C. Yi, J. Luo, J.-D. Décoppet, F. Zhang, S.M. Zakeeruddin, X. Li, A. Hagfeldt, M. Grätzel, Nat. Energy 1 (2016) 16142.
[38] Y. Shi, Y. Xing, Y. Li, Q. Dong, K. Wang, Y. Du, X. Bai, S. Wang, Z. Chen, T. Ma, J. Phys. Chem. C 119 (2015) 15868.
[39] A.G. Thomas, M.J. Jackman, M. Wagstaffe, H. Radtke, K. Syres, J. Adell, A. Lévy, N. Martsinovich, Langmuir 30 (2014) 12306.
[40] D.S. Lee, J.S. Yun, J. Kim, A.M. Soufiani, S. Chen, Y. Cho, X. Deng, J. Seidel, S. Lim, S. Huang, ACS Energy Lett. 3 (2018) 647.
[41] J.-J. Li, J.-Y. Ma, Q.-Q. Ge, J.-S. Hu, D. Wang, L.-J. Wan, ACS Appl. Mater. Interfaces 7 (2015) 28518.
[42] D.H. Cao, C.C. Stoumpos, O.K. Farha, J.T. Hupp, M.G. Kanatzidis, J. Am. Chem. Soc. 137 (2015) 7843.
[43] H.-C. Kwon, A. Kim, H. Lee, D. Lee, S. Jeong, J. Moon, Adv. Energy Mater. 6 (2016) 1601055.
[44] S. Ma, J. Ahn, Y. Oh, H.-C. Kwon, E. Lee, K. Kim, S.-C. Yun, J. Moon, ACS Appl. Mater. Interfaces 10 (2018) 14649.
[45] C. Liu, Z. Huang, X. Hu, X. Meng, L. Huang, J. Xiong, L. Tan, Y. Chen, ACS Appl. Mater. Interfaces 10 (2018) 1909.
[46] S. Wang, Y. Jiang, E.J. Juarez-Perez, L.K. Ono, Y. Qi, Nat. Energy 2 (2017) 16195.
[47] X. Li, C.C. Chen, M. Cai, X. Hua, F. Xie, X. Liu, J. Hua, Y.T. Long, H. Tian, L. Han,

Adv. Energy Mater. (2018) 1800715.

[48] H.-C. Kwon, W. Yang, D. Lee, J. Ahn, E. Lee, S. Ma, K. Kim, S.-C. Yun, J. Moon, ACS Nano 12 (2018) 4233.

[49] G. Niu, W. Li, F. Meng, L. Wang, H. Dong, Y. Qiu, J. Mater. Chem. A 2 (2014) 705.
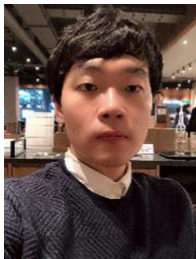
Seong-Cheol Yun received his B.S. degree from the Department of Materials Science and Engineering, Yonsei University, South Korea in 2017. He has received master's degree from Yonsei University under the supervision of Prof. Jooho Moon. His current research focuses on the organometal halide perovskite solar cells.

Sunihl Ma received his B.S. degree in Department of Materials Science and Engineering, Yonsei University, South Korea in 2016. He is a now a Ph.D. candidate in Yonsei University under the supervision of Prof. Jooho Moon. His current research focuses on the fabricating and analyzing the 1-D nanostructured inorganic metal halide perovskite solar cells.
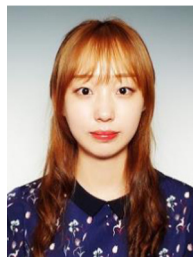
Hyeok-Chan Kwon received his B.S degree in Department of Materials Science and Engineering, Yonsei University, South Korea in 2014. He is currently a Ph.D. student in Yonsei University under the supervision of Prof. Jooho Moon. His research has been focused on the fabricating and analyzing the 1-D nanostructured organometal halide perovskite solar cells.

Kyungmi Kim has received her master's degree from Yonsei University, South Korea in 2018. She is interested in fabricating solution-processed copper nanowire for organometal halide perovskite solar cells.

Gyumin Jang received his B.S. degree from Department of Materials Science and Engineering, Yonsei University, South Korea in 2018. He is currently a Ph.D. student in Yonsei University under the supervision of Prof. Jooho Moon. His research has been focused on application of highly orientation aligned organometal halide perovskite for solar cells.

Hyunha Yang received his B.S. degree from Department of Materials Science and Engineering, Yonsei University, South Korea in 2018. She is currently a candidate of master's degree at the Materials Science and Engineering, Yonsei University. Her research interests focused on fabricating solution-processed nanowire for organometal halide perovskite solar cells.

Prof. Jooho Moon is a professor in the Department of Materials Science and Engineering at Yonsei University, Seoul, Korea. He holds an MS and a Ph.D. in materials science and engineering from the University of Florida. He did his postdoctoral research in the Materials Processing Center at MIT from 1996 to 1998. His research interests include printed electronics and displays, solid oxide fuel cells, perovskite solar cells, and photoelectrochemical water splitting. He has co-authored more than 230 publications in peer-reviewed journals and he is also serving as an associate editor of *ACS Applied Materials & Interface* since 2015.